Advanced Ultrathin RuPdM (M = Ni, Co, Fe) Nanosheets Electrocatalyst Boosts Hydrogen Evolution

Dan Zhang,[†,⊥] Huan Zhao,[†,⊥] Bolong Huang,[‡,⊥] Bin Li,[§] Hongdong Li,[†] Yi Han,[†] Zuochao Wang,[†] Xueke Wu,[†] Yue Pan,[†] Yingjun Sun,[†] Xuemei Sun,[†] Jianping Lai,*[,†] and Lei Wang*[,†]

[†]Key Laboratory of Eco-Chemical Engineering, Taishan Scholar Advantage and Characteristic Discipline Team of Eco-Chemical Process and Technology, College of Chemistry and Molecular Engineering, Qingdao University of Science and Technology, Qingdao 266042, P. R. China

[‡]Department of Applied Biology and Chemical Technology, The Hong Kong Polytechnic University, Hung Hom, Kowloon, Hong Kong SAR, P. R. China

[§]College of Materials Science and Engineering, Qingdao University of Science and Technology, Qingdao 266042, P. R. China

S *Supporting Information*

ABSTRACT: The hydrogen evolution reaction (HER) is one of the most significant reactions in the electrolysis water process, and electrocatalysts which possess high mass activity and excellent stability are the most important driving factors to improve the efficiency of HER. As for the efficient commercially electrocatalyst, Pt/C is limited in development because of its high cost. Therefore, the study of non-Pt high-efficiency catalysts is particularly important at this moment. Here, we creatively report for the first time a kind of RuPdM (M= Ni, Co, Fe) ultrathin nanosheets (NSs), which exhibit extraordinary electrochemical properties for HER under alkaline conditions. The overpotential of optimized trimetallic $Ru_{38}Pd_{34}Ni_{28}$ ultrathin NSs is only 20 mV (10 mA cm^{-2}), and the mass activity reaches 6.15 A $mg^{-1}_{noble\ metal}$ at −0.07 V vs RHE. It can be compared to Pt-based electrocatalysts, which have the highest mass activity currently reported. The durability tests also prove that the stability of the electrocatalyst is outstanding. DFT calculations disclose that the flexible modulation of electronic structures of RuPd ultrathin NSs is achieved by utilizing the additional 3d transition metals Fe, Co, and Ni. In particular, the Ni-3d bands act as the continuous electron-supply center for Ru to ensure an efficient electron transfer toward the adsorbates. Meanwhile, the stable Pd sites are critical for coupling the O-2pπ orbital in the initial H_2O splitting with a facile barrier. This work will open up a new era of non-Pt materials for alkaline hydrogen evolution toward practical application.

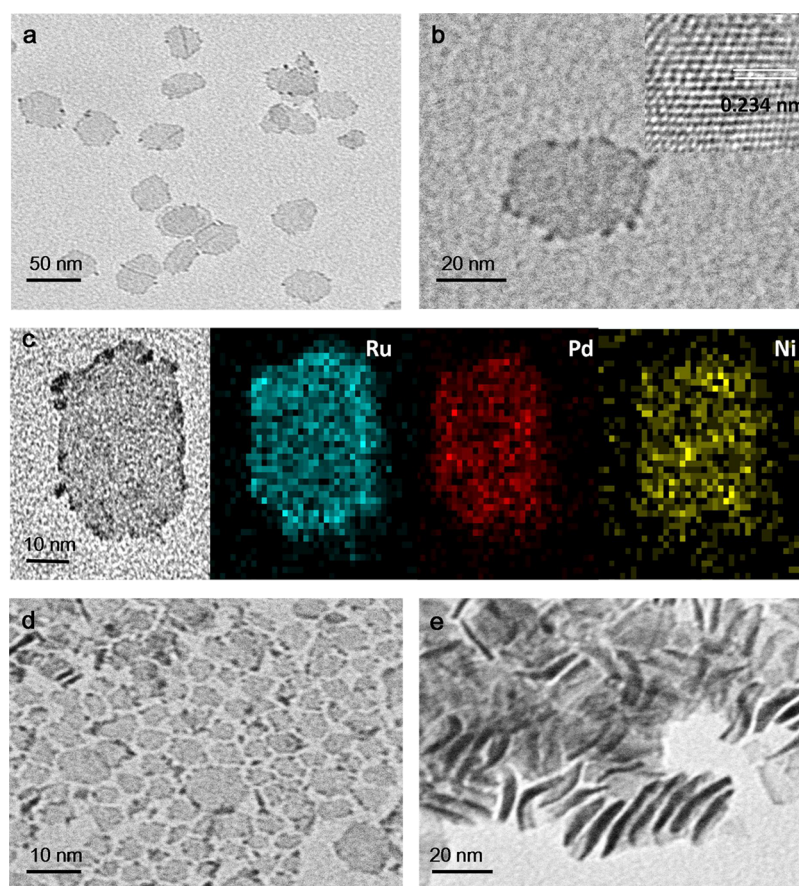$Ru_{38}Pd_{34}Ni_{28}$ ultra-thin NSs
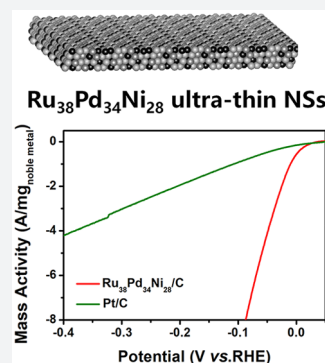
INTRODUCTION

Nowadays, people's demand for energy mainly depends on fossil energy. Coal and oil are the most important energy sources, but they bring many environmental pollution problems, such as global warming, air pollution, and resource exhaustion, which have become a great challenge for human's survival.[1,2] Hydrogen energy as a clean, renewable resource can effectively alleviate the above environmental and resource problems, so hydrogen energy research is extremely urgent.[3−7] In recent years, many novel routes for generating hydrogen have been developed, such as photolysis[8−11] or electrolysis[12−14] of water to produce hydrogen. Among these approaches, electrocatalysis by virtue of the convenience and nonpolluting gas emissions have won the favor of many researchers.[15−17] The hydrogen evolution reaction (HER) is the cathodic reaction in the process of water splitting. The long life of alkaline electrolysis and the simple composition of an electrolytic cell make producing hydrogen from electrolyzed water in alkaline solution meaningful and significant.[18−20] However, the kinetics in alkaline solution is 2−3 orders of magnitude smaller than in acidic solution;[21−23] therefore,

alkaline HER is still faced with great challenges. As the core link in the electrolysis process, many kinds of electrocatalysts have been reported in different literature.[24−28] Compared with them, Pt is still the most effective electrocatalyst in HER,[19,29] but the excessively high price of Pt-based electrocatalysts and ordinary stability limit its future development.

Among various non-Pt electrocatalysts, Ru-based and Pd-based materials are considered to be desirable basic hydrogen evolution catalysts because of their favorable hydrogen bonding energy.[30−32] For instance, Li et al. found that the hydrolysis energy barrier of $RuCo_1$ (19.28 kcal mol^{-1}) is smaller than Ru (26.48 kcal mol^{-1}), $RuCo_2$ (23.01 kcal mol^{-1}), and $RuCo_3$ (21.89 kcal mol^{-1}), because the enhanced OH-bond energy caused an increase in the charge density of the target point around Co atom and results in sluggish water dissociation kinetics, which in turn affected the activity of the active sites.[33] Xu and colleagues prepared $Pd/FeO_x(OH)_{2-2x}$ nanoparticles with a core−shell structure. Experiments showed

Figure 1. (a) TEM image of $Ru_{38}Pd_{34}Ni_{28}$ ultrathin NSs. (b) HRTEM images of $Ru_{38}Pd_{34}Ni_{28}$ ultrathin NSs (the lattice spacing insert). (c) Corresponding TEM mapping of $Ru_{38}Pd_{34}Ni_{28}$ ultrathin NSs. (d) TEM image of $Ru_{40}Pd_{31}Fe_{29}$ ultrathin NSs and $Ru_{37}Pd_{32}Co_{31}$ ultrathin NSs (e).

that the activity of HER has a volcanic shape correlation with the coverage of $FeO_x(OH)_{2-2x}$. The H adsorption and H desorption signals on the surface of $Pd/FeO_x(OH)_{2-2x}$ are stronger than Pd. The results further disclosed the dissociation and transfer process of water.[34] Further progress has been developing, but there is still much room for exploration in designing and synthesizing alkaline HER non-Pt electrocatalysts with high mass activity and outstanding stability. Structurally, the 2D materials have a larger contact area when combined with the carbon materials than 1D nanowires or 0D nanoparticles, so that they could improve the stability of electrocatalysts and increase the electron transfer rate better.[35−37] In addition, ultrathin (<2 nm) structural properties allow exposing more active sites.[38−40]

Here, we successfully synthesized RuPdM (M = Ni, Fe, Co) ultrathin nanosheets(NSs) by a wet chemical method for the first time. These nanostructures have ultrathin nanosized, 2D sheet-like structures and multimetal components. They show excellent electrocatalytic activity and stability in alkaline HER; further, optimized $Ru_{38}Pd_{34}Ni_{28}$ ultrathin NSs exhibits the highest electrocatalytic mass activity, and the hydrogen evolution mass activity in 1.0 M KOH solution reaches 6.15 A $mg^{-1}_{noble\ metal}$ at −0.07 V vs RHE. It is 9.6 times better than Pt/C, 88 times better than Pd/C. It is the highest mass activity among the non-Pt electrocatalysts reported so far. Moreover, after 10 000 cycles of cyclic voltammetry (CV) test, the attenuation of catalytic activity is basically negligible. DFT calculations indicate significant modulation by the introduction of three transition metals to RuPd NSs, in which Ni acts as the

electron pump toward Ru activated highly efficient alkaline HER. The introduction of noble metal Pd enhances the strong p−d coupling between Pd and H_2O and guarantees the efficient water dissociation selectivity in 1.0 M KOH.

RESULTS AND DISCUSSION

Synthesis of $Ru_{38}Pd_{34}Ni_{28}$ Ultrathin NSs. The $Ru_{38}Pd_{34}Ni_{28}$ ultrathin NSs were synthesized by a one-step route. In a typical synthesis method, palladium(II) acetylacetonate $(Pd(acac)_2)$, tridecacarbonyl triazine $(Ru_3(CO)_{12})$, nickel(II) acetylacetonate $(Ni(acac)_2)$, molybdenum carbonyl $(Mo(CO)_6)$, and oleylamine (OA) were placed in a sealed pressure-resistant vial, sonicated for 30 min, and finally formed into a dark brown mixture. The solution was heated to 180 °C from room temperature under magnetic stirring and held for 2 h. Then the final black gelatinous products were collected by centrifugation and stored in cyclohexane for further use (detailed synthetic procedures are summarized in the Supporting Information). No unexpected or unusually high safety hazards were encountered. Transmission electron microscopy (TEM) was first used to characterize the prepared $Ru_{38}Pd_{34}Ni_{28}$ ultrathin NSs. As shown in Figure 1a, the obtained $Ru_{38}Pd_{34}Ni_{28}$ ultrathin NSs possessed a 2D sheet structure. High-resolution TEM (HRTEM) (Figure 1b) shows that the gained $Ru_{38}Pd_{34}Ni_{28}$ ultrathin NSs exhibited high crystallinity and lattice spacing (0.224 nm) is clearly visible. Furthermore, the thickness is about 1.60 nm on average (Figure S1), approximately about six-atom layers, being consistent with the thickness of the nanosheets obtained
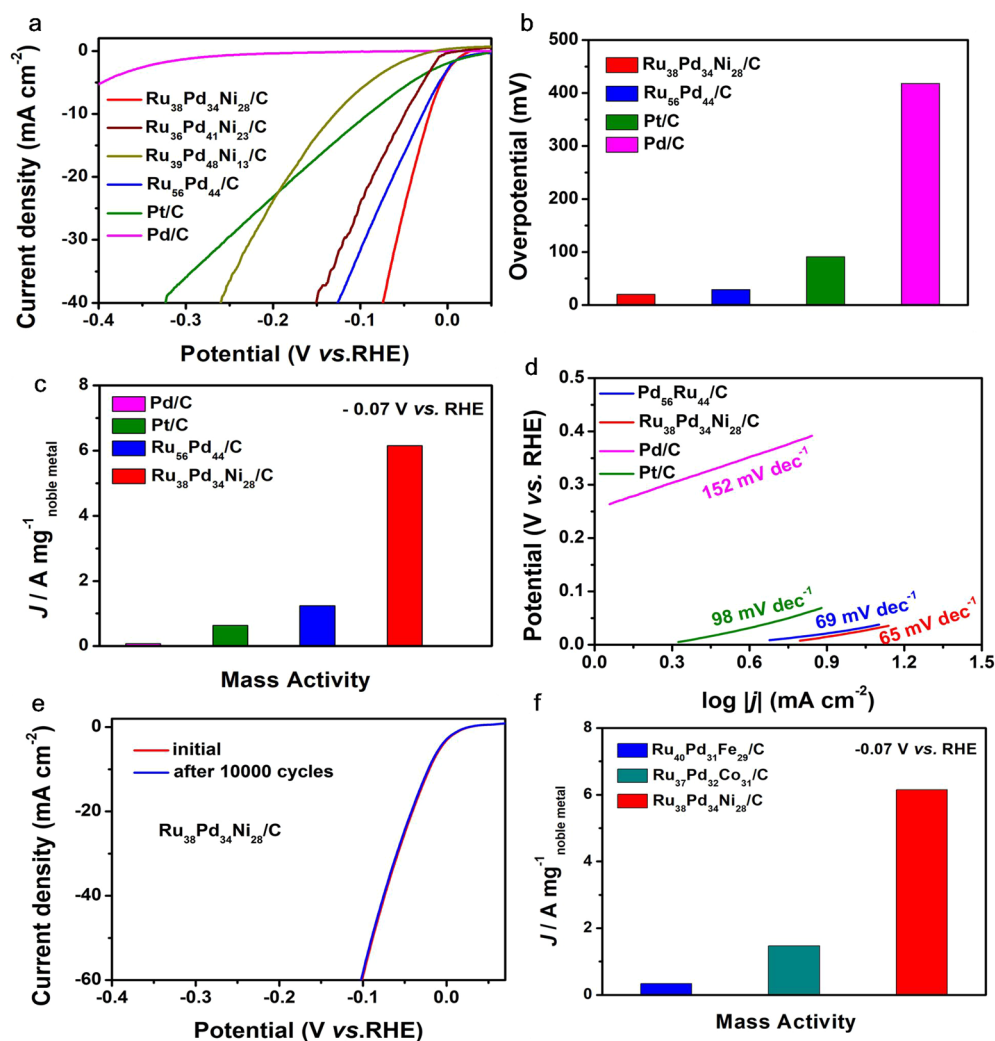
Figure 2. (a) HER polarization curves of $Ru_{38}Pd_{34}Ni_{28}/C$, $Ru_{36}Pd_{41}Ni_{23}/C$, $Ru_{39}Pd_{48}Ni_{13}/C$, $Ru_{56}Pd_{44}/C$, Pt/C, Pd/C. (b) Overpotential of different electrocatalysts at 10 mA cm^{-2}. The HER polarization curves were recorded at room temperature in 1.0 M KOH solution. (c) Mass activities of different electrocatalysts at −0.07 V vs RHE. (d) Tafel plots for the $Ru_{56}Pd_{44}/C$, $Ru_{38}Pd_{34}Ni_{28}/C$, Pd/C, Pt/C. (e) Polarization curves of the $Ru_{38}Pd_{34}Ni_{28}/C$ before and after the 10 000-cycle CV test. (f) Mass activity at −0.07 V vs RHE of prepared $Ru_{37}Pd_{32}Co_{31}/C$, $Ru_{38}Pd_{34}Ni_{28}/C$, and $Ru_{40}Pd_{31}Fe_{29}/C$.

from atomic force microscopy (AFM) (Figure S2a). In addition, the TEM mapping (Figure 1c) shows that the Ru, Pd, and Ni elements are uniformly dispersed on the nanosheets. The XRD spectrum (Figure S2b) shows that the peaks of $Ru_{38}Pd_{34}Ni_{28}$ ultrathin NSs correspond well to the peaks of Pd (JCPDS No. 46-1043). The characteristic peak at 40.11° is attributed to the (111) plane of Pd, and the formation of broad peak is because of the extremely small and thin nanosheets. The peaks of Ni and Ru are not obvious, indicating that the synthesized $Ru_{38}Pd_{34}Ni_{28}$ ultrathin NSs material is well mixed in nanometer size and the (111) crystal plane is dominant.

The synthesis of Pd ultrathin NSs (Figure S3), $Ru_{56}Pd_{44}$ ultrathin NSs (Figure S4), $Ru_{40}Pd_{31}Fe_{29}$ ultrathin NSs (Figure 1d and Figures S5, S6) and $Ru_{37}Pd_{32}Co_{31}$ ultrathin NSs (Figure 1e and Figures S7, S8) are similar to $Ru_{38}Pd_{34}Ni_{28}$ ultrathin NSs (detailed synthetic procedures are summarized in the Supporting Information). However, Ru NSs cannot be synthesized by this method (Figure S9). By changing the molar ratio of $Ni(acac)_2$ and $Pd(acac)_2$, we also obtained $Ru_{39}Pd_{48}Ni_{13}$ ultrathin NSs (Figure S10) and $Ru_{36}Pd_{41}Ni_{23}$

ultrathin NSs (Figure S11) with different Ru, Pd, and Ni elemental compositions. These obtained RuPdM ultrathin NSs were quantitatively analyzed by inductively coupled plasma atomic emission spectroscopy (ICP-AES) analysis and matched with EDX analysis.

The valence state of each element in $Ru_{38}Pd_{34}Ni_{28}$ ultrathin NSs is analyzed by X-ray photoelectron spectroscopy (XPS). It also shows that all three metals are present in the synthesized nanosheets material. Figure S12 shows that the dominant peaks of Pd $3d_{3/2}$ and Pd $3d_{5/2}$ are located at 335.7 and 341.1 eV, which are characteristic peaks attributed to Pd^0. The positions of these two peaks are negatively shifted about 0.5 eV compared with those reported in the literature.[41] The peaks at 336.8 and 342.2 eV belong to Pd^{2+}.[41] The spectrum of Ni 2p shows that the dominant peaks at 855.5 and 872.6 eV, correspond to Ni $2p_{3/2}$ and Ni $2p_{1/2}$, respectively, and the peaks at 855.5 and 872.6 eV are attributed to Ni^0. Peaks at the center of 857.2 and 874.7 eV are attributed to Ni^{2+}. These peaks of Ni 2p are all positively shifted about 0.6 eV.[42] The 3p spectrum of Ru shows two peaks of 461.2 and 483.8 eV, which are attributed to Ru $3p_{3/2}$ and Ru $3p_{1/2}$, respectively. The peaks
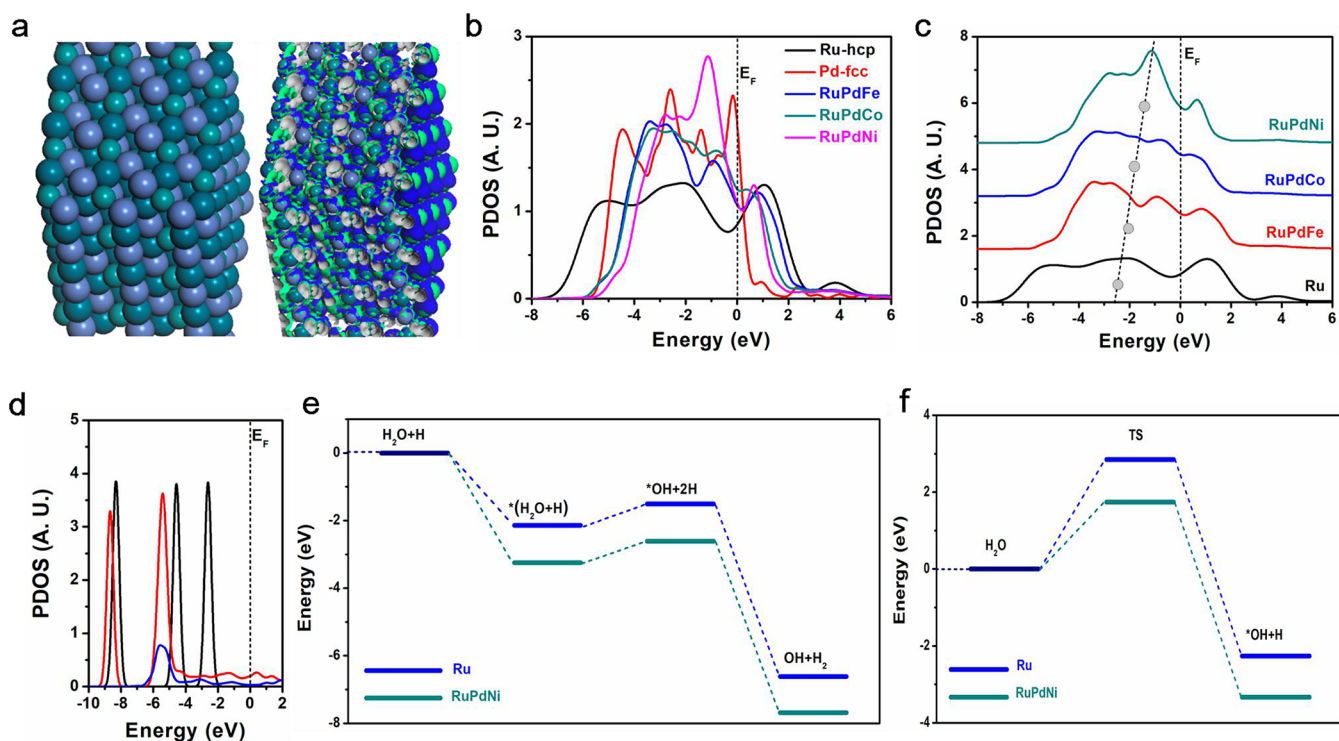
Figure 3. (a) Model of RuPdM ultrathin NSs (M = Ni, Co, Fe). (b) PDOS of Ru, Pd ultrathin NSs, $Ru_{40}Pd_{31}Fe_{29}$ ultrathin NSs, $Ru_{37}Pd_{32}Co_{31}$ ultrathin NSs, $Ru_{38}Pd_{34}Ni_{28}$ ultrathin NSs. (c) More specific PDOS of $Ru_{40}Pd_{31}Fe_{29}$ ultrathin NSs, $Ru_{37}Pd_{32}Co_{31}$ ultrathin NSs, $Ru_{38}Pd_{34}Ni_{28}$ ultrathin NSs. (d) PDOS of H_2O, H, and OH. (e) The pathways of both Ru and RuPdNi ultrathin NSs. (f) Calculated corresponding energy diagram of Ru and $Ru_{38}Pd_{34}Ni_{28}$ ultrathin NSs.

of Ru 3p are all negatively shifted about 0.3 eV,[43] which further proves the electronic relationship between Pd, Ru, and Ni in $Ru_{38}Pd_{34}Ni_{28}$ ultrathin NSs.

Catalytic Performances of Electrocatalyst. In order to evaluate the HER properties of these nanosheets, we performed electrochemical performance characterization in 1.0 M KOH solution. The synthesized ultrathin NSs were combined with Ketjen black to form a catalyst solution of 1 mg mL^{-1} (Figure S13). Catalysts were first activated by CV and the scan rate was 5 mV s^{-1}. Figure 2a shows the polarization curves of Pt/C, Pd/C, $Ru_{56}Pd_{44}$/C, $Ru_{38}Pd_{34}Ni_{28}$/C, $Ru_{36}Pd_{41}Ni_{23}$/C, and $Ru_{39}Pd_{48}Ni_{13}$/C after iR compensation. $Ru_{38}Pd_{34}Ni_{28}$/C has the lowest initial potential and the largest current density. When the current density is 10 mA cm^{-2}, the overpotential of $Ru_{38}Pd_{34}Ni_{28}$/C is only 20 mV, 9 mV lower than $Ru_{56}Pd_{44}$/C (29 mV), 71 mV lower than Pt/C (91 mV), and 398 mV better than Pd/C (418 mV) (Figure 2b). It can be seen that the introduction of transition metals can significantly improve the electrochemical properties of electrocatalysis. RuPdNi/C exhibits increasing catalytic properties by adding the proportions of Pd and Ni. This phenomenon also indicated that the catalytic activities of RuPdNi/C are closely related to the composition (Figure S14). Figure S15a compared their mass current density. Furthermore, Figure 2c also exhibits that the mass current density of $Ru_{38}Pd_{34}Ni_{28}$/C at −0.07 V vs RHE is 6.15 A mg^{-1} $_{noble\ metal}$, 4.91 A mg^{-1} $_{noble\ metal}$ higher than $Ru_{56}Pd_{44}$/C (1.24 A mg^{-1} $_{noble\ metal}$), 5.51 A mg^{-1} $_{noble\ metal}$ higher than Pt/C (0.64 A mg^{-1} $_{Pt}$), and 6.08 A mg^{-1} $_{noble\ metal}$ better than Pd/C (0.07 A mg^{-1} $_{Pd}$). It is indicated that the HER activity of $Ru_{38}Pd_{34}Ni_{28}$/C under alkaline conditions is higher than commercial Pt/C and most alkaline hydrogen evolution materials (Table S2). The Tafel slope is also minimal (Figure

2d). The TOF reaches 12.5, 2.9, 2.28, and 0.68 s^{-1} at 200 mV, corresponding to $Ru_{38}Pd_{34}Ni_{28}$/C, $Ru_{56}Pd_{44}$/C, Pt/C, and Pd/C, respectively (Figure S16). The H_2 produced during the reaction was collected and tested by gas chromatography. The data shows that the measured H_2 value is almost identical to the theoretical value, and the Faraday efficiency is closed to 100% (Figure S17).

Additionally, stability is also an important indicator for evaluating electrocatalysts. The stability of $Ru_{38}Pd_{34}Ni_{28}$/C was tested at the potential of 42 mV (Figure S18a). The time versus voltage curve shows that after 24 h, the potential reveals only a slight attenuation. After the 10 000-cycle CV test, the offset of the polarization curve is basically negligible (Figure 2e). It proves that $Ru_{38}Pd_{34}Ni_{28}$/C has excellent stability. After the stability test, we analyzed the change in the content of each metal element by the ICP-AES test. The results show that only the Ni content is slightly reduced, which may be immersed in the electrolyte. Subsequently, we conducted TEM, HRTEM, XRD, and XPS characterizations of the electrocatalyst after stability test (Figures S19 and S20), and found that the structure did not exhibit particular changes.

Further, we compared the HER performance of $Ru_{38}Pd_{34}Ni_{28}$/C, $Ru_{37}Pd_{32}Co_{31}$/C, $Ru_{40}Pd_{31}Fe_{29}$/C (Figure 2f). At −0.07 V vs RHE, the mass current density of $Ru_{37}Pd_{32}Co_{31}$/C, $Ru_{40}Pd_{31}Fe_{29}$/C are 1.47 A mg^{-1} $_{noble\ metal}$ and 0.33 A mg^{-1} $_{noble\ metal}$ (Figure S21), respectively. The activity is not as good as $Ru_{38}Pd_{34}Ni_{28}$/C. Their stabilities were also tested (Figure S22), and the results show that after the 10 000-cycle CV test, the polarization curves slightly shift, but the degree of shift is negligible. In any case, the mass current densities of all RuPdM/C materials are much higher than commercial Pt/C. The above electrocatalytic properties

indicated that the ternary nanosheets we designed have awesome HER performance in 1.0 M KOH. Experiments also found that $Ru_{38}Pd_{34}Ni_{28}/C$ has a larger electrochemical double layer capacitance (EdlC) (4.8 mF cm^{-2}) than other synthetic materials, indicating that it has a larger electrochemically active surface area (Figures S23 and S24).

DFT was used to investigate the introduction of transition metal (Fe, Co, and Ni) and Pd metal to Ru in facilitating the alkaline HER (Figure 3). The model of RuPdM (M = Fe, Co and Ni) shows an interlayer distance of 16.8 Å, which is highly consistent with the experimental AFM results of 1.60 nm. The surface-active bonding and antibonding orbitals near the Fermi level (E_F) have been illustrated for addressing effective modifications of Ni, which leads to the evident surface electron-rich feature (Figure 3a). The modulations originated from the introduction of the third transition metals are also illustrated by the normalized partial density of states (PDOS). From Fe to Ni, varied changes in electronic structures are noted, indicating different levels of modification of electroactivity (Figure 3b). More specifically, a linear shifting up of d-band center is clearly demonstrated, in which the d-band has been uplifted from E_v of −2.5 eV toward E_v of −1.5 eV, representing a gradual activation of electroactivities in RuPdM (Figure 3c). Then, we move to the detailed PDOS of each RuPdM. In RuPdFe, the e_g-t_{2g} component of surface Fe-site stays at E_v of −3 eV and E_v of +1 eV, respectively. Meanwhile, the Ru-4d bands are located at the center between Pd-4d and Fe-3d bands, representing a stable valence of Ru is preserved by shielding from Pd and Fe (Figure S25a). In contrast, a good coupling between Ru and Co in RuPdCo has been observed, which averages the band-center position to avoid the overbinding effect (Figure S25b). Most importantly, the substantial electron boost is achieved by the "electron pump" Ni-3d bands, which exhibit high occupation of electrons near E_F. The continuous electron supply from Ni guarantees the highest electroactivity toward alkaline HER (Figure S25c). The electronic structures of key intermediates in alkaline HER are also critical in determining efficiency. The initial reactant H_2O displays the dominant peak at E_v of −3.0 eV, which is well-matched with Pd-4d bands for achieving a facile water dissociation. The PDOS of formed *OH shifted toward a lower position than Pd-4d bands. The blocking effect of Pd-4d bands significantly alleviates the overbinding effect that hinders the formation of H_2. A similar PDOS occupation is noted in *H that supports the high electroactivity of H_2 formation (Figure 3d). From the energetic view, the pathways of both Ru and RuPdNi ultrathin NSs indicate a 0.50 eV barrier at the initial [H_2O* + H → *OH + 2H]. However, the larger overall energy release of RuPdNi demonstrates a stronger physicochemical trend of alkaline HER (Figure 3e). The activation barrier of H_2O-splitting behavior illustrates the RuPdNi system significantly minimizes the barrier from 2.80 to 1.70 eV of the pristine Ru surface, being a more energetic favorable trend for alkaline HER (Figure 3f).

CONCLUSIONS

In summary, by systematically engineering the electronic structures and material morphology of non-Pt electrocatalyst, the RuPdM (Fe, Co, Ni) ultrathin NSs possess excellent mass catalytic activity under alkaline condition. Additionally, the regulation of the composition ratio allowed us to select the most active element ratio. Trimetallic $Ru_{38}Pd_{34}Ni_{28}/C$, as the most extraordinary electrocatalyst under alkaline conditions,

achieved the maximum mass activity among non-Pt catalysts reported so far. Furthermore, the activity decay was particularly slow after a long period of stability test. The simultaneous contributions by multitransition metals supply a practical strategy to achieve flexible electroactivity tuning of nanosheets. In particular, the Ni-3d bands act as the pivotal "electron-pump" to boost the Ru-4d bands in actualizing highly efficient alkaline HER. Meanwhile, the lower activation barrier of initial water splitting is another key factor to ensure the high efficiency and selectivity of alkaline HER, which is induced by the substantial coupling between pinned Pd-4d bands and H_2O. This work will open up a new era of non-Pt materials for alkaline hydrogen evolution toward practical application.

■ ASSOCIATED CONTENT

ⓢ Supporting Information

The Supporting Information is available free of charge at https://pubs.acs.org/doi/10.1021/acscentsci.9b01110.

Experimental details, electrochemical test method, TEM images, and additional data (PDF)

■ AUTHOR INFORMATION

Corresponding Authors
*(J.L.) E-mail: jplai@qust.edu.cn.
*(L.W.) E-mail: inorchemwl@126.com.

ORCID Ⓘ
Bolong Huang: 0000-0002-2526-2002
Lei Wang: 0000-0001-7275-4846

Author Contributions
⊥D.Z., H.Z., and B.H. contributed equally.

Notes
The authors declare no competing financial interest.

■ REFERENCES

(1) Chu, S.; Majumdar, A. Opportunities and challenges for a sustainable energy future. *Nature* **2012**, *488*, 294−303.

(2) Zhao, G.; Rui, K.; Dou, S. X.; Sun, W. Heterostructures for electrochemical hydrogen evolution reaction: A review. *Adv. Funct. Mater.* **2018**, *28*, 1803291.

(3) Zang, Y.; Niu, S.; Wu, Y.; Zheng, X.; Cai, J.; Ye, J.; Xie, Y.; Liu, Y.; Zhou, J.; Zhu, J.; Liu, X.; Wang, G.; Qian, Y. Tuning orbital orientation endows molybdenum disulfide with exceptional alkaline hydrogen evolution capability. *Nat. Commun.* **2019**, *10*, 1217.

(4) Ling, T.; Zhang, T.; Ge, B.; Han, L.; Zheng, L.; Lin, F.; Xu, Z.; Hu, W.-B.; Du, X.-W.; Davey, K.; Qiao, S.-Z. Well-dispersed nickel- and zinc-tailored electronic structure of a transition metal oxide for highly active alkaline hydrogen evolution reaction. *Adv. Mater.* **2019**, *31*, 1807771.

(5) Huang, Y.; Sun, Y.; Zheng, X.; Aoki, T.; Pattengale, B.; Huang, J.; He, X.; Bian, W.; Younan, S.; Williams, N.; Hu, J.; Ge, J.; Pu, N.; Yan, X.; Pan, X.; Zhang, L.; Wei, Y.; Gu, J. Atomically engineering activation sites onto metallic 1T-MoS_2 catalysts for enhanced electrochemical hydrogen evolution. *Nat. Commun.* **2019**, *10*, 982.

(6) Turner, J. A. Sustainable hydrogen production. *Science* **2004**, *305*, 972−974.

(7) Baek, D. S.; Jung, G. Y.; Seo, B.; Kim, J. C.; Lee, H.-W.; Shin, T. J.; Jeong, H. Y.; Kwak, S. K.; Joo, S. H. Ordered mesoporous metastable α-MoC$_{1-x}$ with enhanced water dissociation capability for boosting alkaline hydrogen evolution activity. *Adv. Funct. Mater.* **2019**, *29*, 1901217.

(8) Zhang, G.; Li, G.; Heil, T.; Zafeiratos, S.; Lai, F.; Savateev, A.; Antonietti, M.; Wang, X. Tailoring the grain boundary chemistry of polymeric carbon nitride for enhanced solar hydrogen production and CO$_2$ reduction. *Angew. Chem.* **2019**, *131*, 3471−3475.

(9) Zhou, G.; Shan, Y.; Hu, Y.; Xu, X.; Long, L.; Zhang, J.; Dai, J.; Guo, J.; Shen, J.; Li, S.; Liu, L.; Wu, X. Half-metallic carbon nitride nanosheets with micro grid mode resonance structure for efficient photocatalytic hydrogen evolution. *Nat. Commun.* **2018**, *9*, 3366.

(10) Zhang, Z.; Zhu, Y.; Chen, X.; Zhang, H.; Wang, J. A full-spectrum metal-free porphyrin supramolecular photocatalyst for dual functions of highly efficient hydrogen and oxygen evolution. *Adv. Mater.* **2019**, *31*, 1806626.

(11) Zhang, H.; Zhang, P.; Qiu, M.; Dong, J.; Zhang, Y.; Lou, X. W. Ultrasmall MoO$_x$ clusters as a novel cocatalyst for photocatalytic hydrogen evolution. *Adv. Mater.* **2018**, *31*, 1804883.

(12) Wu, W.; Niu, C.; Wei, C.; Jia, Y.; Li, C.; Xu, Q. Activation of MoS$_2$ basal planes for hydrogen evolution by zinc. *Angew. Chem., Int. Ed.* **2019**, *58*, 2029−2033.

(13) Zang, X.; Chen, W.; Zou, X.; Hohman, J. N.; Yang, L.; Li, B.; Wei, M.; Zhu, C.; Liang, J.; Sanghadasa, M.; Gu, J.; Lin, L. Self-assembly of large-area 2D polycrystalline transition metal carbides for hydrogen electrocatalysis. *Adv. Mater.* **2018**, *30*, 1805188.

(14) You, B.; Liu, X.; Hu, G.; Gul, S.; Yano, J.; Jiang, D.-e.; Sun, Y. Universal surface engineering of transition metals for superior electrocatalytic hydrogen evolution in neutral water. *J. Am. Chem. Soc.* **2017**, *139*, 12283−12290.

(15) Lai, J.; Huang, B.; Chao, Y.; Chen, X.; Guo, S. Strongly coupled nickel-cobalt nitrides/carbon hybrid nanocages with Pt-like activity for hydrogen evolution catalysis. *Adv. Mater.* **2019**, *31*, 1805541.

(16) Seh, Z. W.; Kibsgaard, J.; Dickens, C. F.; Chorkendorff, I.; Nørskov, J. K.; Jaramillo, T. F. Combining theory and experiment in electrocatalysis: Insights into materials design. *Science* **2017**, *355*, eaad4998.

(17) Lai, J.; Huang, B.; Tang, Y.; Lin, F.; Zhou, P.; Chen, X.; Sun, Y.; Lv, F.; Guo, S. Barrier-free interface electron transfer on PtFe-Fe$_2$C janus-like nanoparticles boosts oxygen catalysis. *Chem.* **2018**, *4*, 1153−1166.

(18) Yin, H.; Zhao, S.; Zhao, K.; Muqsit, A.; Tang, H.; Chang, L.; Zhao, H.; Gao, Y.; Tang, Z. Ultrathin platinum nanowires grown on single-layered nickel hydroxide with high hydrogen evolution activity. *Nat. Commun.* **2015**, *6*, 6430.

(19) Wang, P.; Jiang, K.; Wang, G.; Yao, J.; Huang, X. Phase and interface engineering of platinum−nickel nanowires for efficient electrochemical hydrogen evolution. *Angew. Chem., Int. Ed.* **2016**, *55*, 12859−12863.

(20) Zheng, Y.; Jiao, Y.; Zhu, Y.; Li, L. H.; Han, Y.; Chen, Y.; Jaroniec, M.; Qiao, S.-Z. High electrocatalytic hydrogen evolution activity of an anomalous ruthenium catalyst. *J. Am. Chem. Soc.* **2016**, *138*, 16174−16181.

(21) Zhu, Z.; Yin, H.; He, C. T.; Al-Mamun, M.; Liu, P.; Jiang, L.; Zhao, Y.; Wang, Y.; Yang, H. G.; Tang, Z.; Wang, D.; Chen, X. M.; Zhao, H. Ultrathin transition metal dichalcogenide/3d metal hydroxide hybridized nanosheets to enhance hydrogen evolution activity. *Adv. Mater.* **2018**, *30*, 1801171.

(22) Yan, H.; Xie, Y.; Jiao, Y.; Wu, A.; Tian, C.; Zhang, X.; Wang, L.; Fu, H. Holey reduced graphene oxide coupled with an Mo$_2$N-Mo$_2$C heterojunction for efficient hydrogen evolution. *Adv. Mater.* **2018**, *30*, 1704156.

(23) Zhang, J.; Wang, T.; Liu, P.; Liao, Z.; Liu, S.; Zhuang, X.; Chen, M.; Zschech, E.; Feng, X. Efficient hydrogen production on MoNi$_4$ electrocatalysts with fast water dissociation kinetics. *Nat. Commun.* **2017**, *8*, 15437.

(24) Lai, J.; Luque, R.; Xu, G. Recent advances in the synthesis and electrocatalytic applications of platinum-based bimetallic alloy nanostructures. *ChemCatChem* **2015**, *7*, 3206−3228.

(25) Jiang, P.; Chen, J.; Wang, C.; Yang, K.; Gong, S.; Liu, S.; Lin, Z.; Li, M.; Xia, G.; Yang, Y.; Su, J.; Chen, Q. Tuning the activity of carbon for electrocatalytic hydrogen evolution via an iridium-cobalt alloy core encapsulated in nitrogen-doped carbonc ages. *Adv. Mater.* **2018**, *30*, 1705324.

(26) Cui, B.; Hu, B.; Liu, J.; Wang, M.; Song, Y.; Tian, K.; Zhang, Z.; He, L. Solution-plasma-assisted bimetallic oxide alloy nanoparticles of Pt and Pd embedded within two-dimensional Ti$_3$C$_2$T$_x$ nanosheets as highly active electrocatalysts for overall water splitting. *ACS Appl. Mater. Interfaces* **2018**, *10*, 23858−23873.

(27) Zhao, Z.; Liu, H.; Gao, W.; Xue, W.; Liu, Z.; Huang, J.; Pan, X.; Huang, Y. Surface-engineered PtNi-O nanostructure with record-high performance for electrocatalytic hydrogen evolution reaction. *J. Am. Chem. Soc.* **2018**, *140*, 9046−9050.

(28) Liu, T.; Li, P.; Yao, N.; Cheng, G.; Luo, W.; Chen, S.; Yin, Y. CoP-doped MOF-based electrocatalyst for pH-universal hydrogen evolution reaction. *Angew. Chem., Int. Ed.* **2019**, *58*, 4679−4684.

(29) Wang, M.; Zhang, W.; Zhang, F.; Zhang, Z.; Tang, B.; Li, J.; Wang, X. Theoretical expectation and experimental implementation of in situ Al-doped CoS$_2$ nanowires on dealloying-derived nanoporous intermetallic substrate as an efficient electrocatalyst for boosting hydrogen production. *ACS Catal.* **2019**, *9*, 1489−1502.

(30) Creus, J.; Drouet, S.; Suriñach, S.; Lecante, P.; Collière, V.; Poteau, R.; Philippot, K.; García-Antón, J.; Sala, X. Ligand-capped Ru nanoparticles as efficient electrocatalyst for the hydrogen evolution reaction. *ACS Catal.* **2018**, *8*, 11094−11102.

(31) Hu, C.; Zhang, L.; Gong, J. Recent progress of mechanism comprehension and design of electrocatalysts for alkaline water splitting. *Energy Environ. Sci.* **2019**, *12*, 2620−2645.

(32) Mitchell, W. J.; Xie, J.; Jachimowski, T. A.; Weinberg, W. H. Carbon monoxide hydrogenation on the Ru (001) surface at low temperature using gas-phase atomic hydrogen: spectroscopic evidence for the carbonyl insertion mechanism on a transition metal surface. *J. Am. Chem. Soc.* **1995**, *117*, 2606−2617.

(33) Mao, J.; He, C.-T.; Pei, J.; Chen, W.; He, D.; He, Y.; Zhuang, Z.; Chen, C.; Peng, Q.; Wang, D.; Li, Y. Accelerating water dissociation kinetics by isolating cobalt atoms into ruthenium lattice. *Nat. Commun.* **2018**, *9*, 4958.

(34) Liao, H.; Wei, C.; Wang, J.; Fisher, A.; Sritharan, T.; Feng, Z.; Xu, Z. J. A multisite strategy for enhancing the hydrogen evolution reaction on a nano-Pd surface in alkaline media. *Adv. Energy Mater.* **2017**, *7*, 1701129.

(35) Wang, L.; Zhang, Y.; Chen, L.; Xu, H.; Xiong, Y. 2D polymers as emerging materials for photocatalytic overall water splitting. *Adv. Mater.* **2018**, *30*, 1801955.

(36) Liu, S.-W.; Wang, H.-P.; Xu, Q.; Ma, T.-B.; Yu, G.; Zhang, C.; Geng, D.; Yu, Z.; Zhang, S.; Wang, W.; Hu, Y.-Z.; Wang, H.; Luo, J. Robust microscale superlubricity under high contact pressure enabled by graphene-coated microsphere. *Nat. Commun.* **2017**, *8*, 14029.

(37) Hong, X.; Tan, C.; Chen, J.; Xu, Z.; Zhang, H. Synthesis, properties and applications of one- and two-dimensional gold nanostructures. *Nano Res.* **2015**, *8*, 40−55.

(38) Tan, C.; Cao, X.; Wu, X.-J.; He, Q.; Yang, J.; Zhang, X.; Chen, J.; Zhao, W.; Han, S.; Nam, G.-H.; Sindoro, M.; Zhang, H. Recent advances in ultrathin two-dimensional nanomaterials. *Chem. Rev.* **2017**, *117*, 6225−6331.

(39) Dou, Y.; Zhang, L.; Xu, X.; Sun, Z.; Liao, T.; Dou, S. X. Atomically thin non-layered nanomaterials for energy storage and conversion. *Chem. Soc. Rev.* **2017**, *46*, 7338−7373.

(40) Yang, W.; Zhang, X.; Xie, Y. Advances and challenges in chemistry of two-dimensional nanosheets. *Nano Today* **2016**, *11*, 793−816.

(41) Yang, X.; Xu, W.; Cao, S.; Zhu, S.; Liang, Y.; Cui, Z.; Yang, X.; Li, Z.; Wu, S.; Inoue, A.; Chen, L. An amorphous nanoporous PdCuNi-S hybrid electrocatalyst for highly efficient hydrogen production. *Appl. Catal., B* **2019**, *246*, 156−165.

(42) Feng, Y.; Yang, C.; Fang, W.; Huang, B.; Shao, Q.; Huang, X. Anti-poisoned oxygen reduction by the interface modulated Pd@NiO core@shell. *Nano Energy* **2019**, *58*, 234−243.

(43) Pu, Z.; Amiinu, I. S.; Kou, Z.; Li, W.; Mu, S. RuP$_2$-based catalysts with platinum-like activity and higher durability for hydrogen evolution reaction at all pH values. *Angew. Chem., Int. Ed.* **2017**, *56*, 11559−11564.